THE EUROPEAN
PHYSICAL JOURNAL C

Precision measurement of the electron energy-loss function in tritium and deuterium gas for the KATRIN experiment

M. Aker[1], A. Beglarian[2], J. Behrens[3,4], A. Berlev[5], U. Besserer[1], B. Bieringer[6], F. Block[4], B. Bornschein[1],
L. Bornschein[3], M. Böttcher[6], T. Brunst[7,8], T. S. Caldwell[9,10], R. M. D. Carney[11], S. Chilingaryan[2], W. Choi[4],
K. Debowski[12], M. Deffert[4], M. Descher[4], D. Díaz Barrero[13], P. J. Doe[14], O. Dragoun[15], G. Drexlin[4], F. Edzards[7,8],
K. Eitel[3], E. Ellinger[12], A. El Miniawy[20], R. Engel[3], S. Enomoto[14], A. Felden[3], J. A. Formaggio[16], F. M. Fränkle[3],
G. B. Franklin[17], F. Friedel[4], A. Fulst[6], K. Gauda[6], W. Gil[3], F. Glück[3], S. Groh[3,4], R. Grössle[1], R. Gumbsheimer[3],
V. Hannen[6], N. Haußmann[12], F. Heizmann[3,4], K. Helbing[12], S. Hickford[4], R. Hiller[4], D. Hillesheimer[1], D. Hinz[3],
T. Höhn[3], T. Houdy[7,8], A. Huber[4], A. Jansen[3], C. Karl[7,8], J. Kellerer[4], M. Kleesiek[3,4], M. Klein[3,4], C. Köhler[7,8],
L. Köllenberger[3], A. Kopmann[2], M. Korzeczek[4], A. Kovalík[15], B. Krasch[1], H. Krause[3], N. Kunka[2], T. Lasserre[18],
L. La Cascio[4], O. Lebeda[15], B. Lehnert[11], T. L. Le[1], A. Lokhov[5,6], M. Machatschek[4], E. Malcherek[3], M. Mark[3],
A. Marsteller[1], E. L. Martin[9,10], M. Meier[7,8], C. Melzer[1], A. Menshikov[2], S. Mertens[7,8], J. Mostafa[2], K. Müller[3],
S. Niemes[1], P. Oelpmann[6], D. S. Parno[17], A. W. P. Poon[11], J. M. L. Poyato[13], F. Priester[1], P. C.-O. Ranitzsch[6],
R. G. H. Robertson[14], W. Rodejohann[19], C. Rodenbeck[6,a], M. Röllig[1], C. Röttele[1], M. Ryšavý[15], R. Sack[3,6],
A. Saenz[20], P. Schäfer[1], A. Schaller (née Pollithy)[7,8], L. Schimpf[4,6,b], K. Schlösser[3], M. Schlösser[1], L. Schlüter[7,8],
S. Schneidewind[6], M. Schrank[3], B. Schulz[20], C. Schwachtgen[4], M. Šefčík[15], H. Seitz-Moskaliuk[4], V. Sibille[16],
D. Siegmann[7,8], M. Slezák[7,8], M. Steidl[3], M. Sturm[1], M. Sun[14], D. Tcherniakhovski[2], H. H. Telle[13], L. A. Thorne[17],
T. Thümmler[3], N. Titov[5], I. Tkachev[5], N. Trost[3,4], K. Urban[7,8], K. Valerius[3], D. Vénos[15],
A. P. Vizcaya Hernández[17], C. Weinheimer[6], S. Welte[1], J. Wendel[1], J. F. Wilkerson[9,10], J. Wolf[4], S. Wüstling[2],
W. Xu[16], Y.-R. Yen[17], S. Zadoroghny[5], G. Zeller[1]

[1] Tritium Laboratory Karlsruhe (TLK), Karlsruhe Institute of Technology (KIT), Hermann-von-Helmholtz-Platz 1, 76344 Eggenstein-Leopoldshafen, Germany
[2] Institute for Data Processing and Electronics (IPE), Karlsruhe Institute of Technology (KIT), Hermann-von-Helmholtz-Platz 1, 76344 Eggenstein-Leopoldshafen, Germany
[3] Institute for Astroparticle Physics (IAP), Karlsruhe Institute of Technology (KIT), Hermann-von-Helmholtz-Platz 1, 76344 Eggenstein-Leopoldshafen, Germany
[4] Institute of Experimental Particle Physics (ETP), Karlsruhe Institute of Technology (KIT), Wolfgang-Gaede-Str. 1, 76131 Karlsruhe, Germany
[5] Institute for Nuclear Research of Russian Academy of Sciences, 60th October Anniversary Prospect 7a, 117312 Moscow, Russia
[6] Institut für Kernphysik, Westfälische Wilhelms-Universität Münster, Wilhelm-Klemm-Str. 9, 48149 Münster, Germany
[7] Technische Universität München, James-Franck-Str. 1, 85748 Garching, Germany
[8] Max-Planck-Institut für Physik, Föhringer Ring 6, 80805 Munich, Germany
[9] Department of Physics and Astronomy, University of North Carolina, Chapel Hill, NC 27599, USA
[10] Triangle Universities Nuclear Laboratory, Durham, NC 27708, USA
[11] Institute for Nuclear and Particle Astrophysics and Nuclear Science Division, Lawrence Berkeley National Laboratory, Berkeley, CA 94720, USA
[12] Department of Physics, Faculty of Mathematics and Natural Sciences, University of Wuppertal, Gaußstr. 20, 42119 Wuppertal, Germany
[13] Departamento de Química Física Aplicada, Universidad Autonoma de Madrid, Campus de Cantoblanco, 28049 Madrid, Spain
[14] Center for Experimental Nuclear Physics and Astrophysics, and Dept. of Physics, University of Washington, Seattle, WA 98195, USA
[15] Nuclear Physics Institute of the CAS, v. v. i., 250 68 Řež, Czech Republic
[16] Laboratory for Nuclear Science, Massachusetts Institute of Technology, 77 Massachusetts Ave, Cambridge, MA 02139, USA
[17] Department of Physics, Carnegie Mellon University, Pittsburgh, PA 15213, USA
[18] IRFU (DPhP & APC), CEA, Université Paris-Saclay, 91191 Gif-sur-Yvette, France
[19] Max-Planck-Institut für Kernphysik, Saupfercheckweg 1, 69117 Heidelberg, Germany
[20] Institut für Physik, Humboldt-Universität zu Berlin, Newtonstr. 15, 12489 Berlin, Germany

Springer

Abstract The KATRIN experiment is designed for a direct and model-independent determination of the effective electron anti-neutrino mass via a high-precision measurement of the tritium β-decay endpoint region with a sensitivity on m_ν of 0.2 eV/c^2 (90% CL). For this purpose, the β-electrons from a high-luminosity windowless gaseous tritium source traversing an electrostatic retarding spectrometer are counted to obtain an integral spectrum around the endpoint energy of 18.6 keV. A dominant systematic effect of the response of the experimental setup is the energy loss of β-electrons from elastic and inelastic scattering off tritium molecules within the source. We determined the energy-loss function in-situ with a pulsed angular-selective and monoenergetic photo-electron source at various tritium-source densities. The data was recorded in integral and differential modes; the latter was achieved by using a novel time-of-flight technique. We developed a semi-empirical parametrization for the energy-loss function for the scattering of 18.6-keV electrons from hydrogen isotopologs. This model was fit to measurement data with a 95% T$_2$ gas mixture at 30 K, as used in the first KATRIN neutrino-mass analyses, as well as a D$_2$ gas mixture of 96% purity used in KATRIN commissioning runs. The achieved precision on the energy-loss function has abated the corresponding uncertainty of $\sigma(m_\nu^2) < 10^{-2}\text{eV}^2$ [1] in the KATRIN neutrino-mass measurement to a subdominant level.

Contents

1 Introduction

The KArlsruhe TRItium Neutrino (KATRIN) experiment aims to determine the effective electron anti-neutrino mass in a model-independent way by examining the kinematics of tritium β-decays. The observable $m_\nu^2 = \sum_i |U_{ei}|^2 m_i^2$ is the squared incoherent sum of neutrino-mass eigenstates m_i weighted by their contribution U_{ei} to the electron anti-neutrino. The target sensitivity for the neutrino-mass measurement in KATRIN is 0.2 eV/c^2 (at 90% CL) with three live-years of data [2]. The 5σ discovery potential is

^{a} e-mail: rodenbeck@wwu.de

^{b} e-mail: lschimpf@wwu.de (corresponding author)

0.35 eV/c^2. This requires a precise control of all systematic effects. The experiment is designed for a high-precision spectral shape measurement of T$_2$ β-decay electrons around the endpoint of 18.6 keV. An overview of the KATRIN experiment is shown in Fig. 1. The setup [3] includes a high-activity Windowless Gaseous Tritium Source (WGTS) and a high-resolution electrostatic retarding spectrometer of the MAC-E (Magnetic Adiabatic Collimation with an Electrostatic filter) type [4–6]. Molecular tritium gas at 30 K is continuously injected through the capillaries at the center of the WGTS and pumped out at both ends. This allows a nominal steady-state column density (i.e. the integrated nominal source density $\rho_0(z)$ along the length d of the source cryostat) $\rho_0 d = 5 \times 10^{17}$cm^{-2} resulting in an activity of 1.7×10^{11}Bq with a stability better than 0.1%h^{-1} [3].

In order to prevent tritium from entering the spectrometer section which would induce background in the measurement, the transport section reduces the tritium flow by at least 14 orders of magnitude [7]. This is achieved with a differential pumping section [3,8], which comprises turbo-molecular pumps followed by a cryogenic pumping section that makes use of an argon frost layer to adsorb tritium cryogenically [3,9]. The spectrometer section consists of the pre- and the main spectrometer. The pre-spectrometer rejects low-energy electrons, which reduces the electron flux into the main spectrometer. The final precision discrimination of the electron energy is performed in the analyzing plane at the center of the main spectrometer with a resolution of 2.77 eV [3] for 18.6-keV electrons with isotropic angular distribution.

The pre- and main spectrometer are MAC-E type high-pass filters, which can only be traversed by electrons with longitudinal kinetic energy higher than the preset potential. The isotropically emitted β-electrons are adiabatically collimated to a longitudinal motion inside the spectrometer. This is achieved by a gradual decrease of the magnetic field strength B from the entrance of the spectrometer towards its center, conserving the magnitude of the β-electron's magnetic moment in the cyclotron motion $\mu = E_\perp/B$ [4], with $E_\perp$ being the transverse component of the electron's kinetic energy with respect to the magnetic field lines. Varying the electric potential of the spectrometer allows the energy region around the endpoint of the tritium β-decay to be scanned as an integral spectrum, i.e. the rate of electrons with kinetic energy above the set filter potential [1].

Electrons passing the main spectrometer are re-accelerated by the main spectrometer potential and a post-acceleration of 10 kV at the focal-plane detector (FPD) system and are then counted by a 148-pixel silicon PIN detector [10] shown at the far right in Fig. 1. An 18-keV-wide selection window (14 keV to 32 keV) around the 28-keV electron energy peak is chosen to minimize systematic effects in counting efficiencies [1].
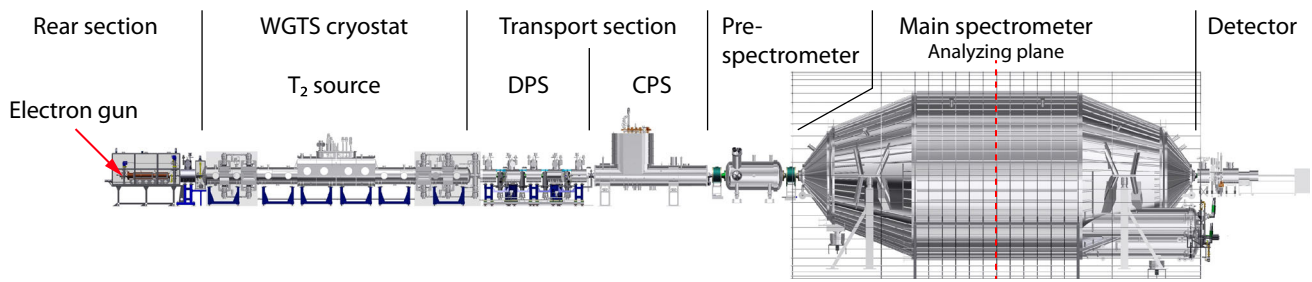
Fig. 1 Overview of the KATRIN experiment. The main components are from left to right: The rear section containing calibration and monitoring systems as well as the electron gun (see Fig. 2) used in this work; the 10-m-long windowless gaseous tritium source (WGTS) with differential pumps on both sides; the transport section consisting of a differential (DPS) and cryogenic pumping section (CPS); the spectrometer and detector section with the pre- and main spectrometer, and the silicon detector. The overall length of the experimental setup is more than 70 m

The observable m_ν^2 is determined by fitting the recorded integral spectrum with a model that comprises four parameters: the normalization, the endpoint energy, the background rate, and m_ν^2 [11]. The model is constructed from the shape of the β-decay spectrum and the response of the experimental setup. The main components of the response are the transmission function of the main spectrometer and the energy loss of electrons from elastic and inelastic scatterings in the T_2 source. The latter is the focus of this work.

At the nominal source density, approximately 60% of all electrons scatter inelastically and lose energies between $\approx 11\,\mathrm{eV}$ and 9.3 keV. The upper limit of this energy transfer arises due to the fact that the primary and secondary electrons from the ionization process are indistinguishable in the measurement and always the higher energetic electron is measured. Minuscule energy losses can result in electrons with energies close to the endpoint downgraded to lower energies in the spectrum fit window. Therefore, the energy-loss function needs to be known with high precision in order to meet the systematic uncertainty budget of $\sigma(m_\nu^2) < 7.5 \times 10^{-3}\mathrm{eV}^2$ [2] reserved for this individual systematic.

Theoretical differential cross sections for 18.6-keV electrons scattering off molecular tritium are not available at the required precision for the m_ν^2 measurements. While data from energy-loss measurements for gaseous tritium or deuterium from the former neutrino mass experiments in Troitsk and Mainz [12,13] exist, the precision is not sufficient to achieve the KATRIN design sensitivities. Other more precise experimental data on the energy losses of electrons with energies near the tritium β-decay endpoint energy are only available for molecular hydrogen as the target gas [13–15]. In this paper we report the results of the in-situ measurements of the energy-loss function in the KATRIN experiment.

We used a monoenergetic and angular-selective electron gun, of the type described in [16], mounted in the rear section (far left in Fig. 1), which allowed us to probe the response of

the entire KATRIN setup, including the energy loss in tritium gas.

We begin this paper in Sect. 2 with a brief introduction to existing energy-loss function models and continue with the description of the novel semi-empirical parametrization developed in this work. In Sect. 3, the measurement approaches of the integral as well as the novel differential time-of-flight measurements are explained, including a description of the working principle of the electron gun used for these measurements. The analysis of the tritium data using a combined fit is presented in Sect. 4 including a detailed discussion of the systematic uncertainties of the measurements. Additional measurement results for the energy-loss function in deuterium gas are provided in Sect. 4.3. We conclude this paper in Sect. 5 by summarizing and discussing our results in the context of the neutrino-mass-sensitivity goal of KATRIN.

2 Energy-loss function

Multiple processes contribute to the energy loss of electrons traversing molecular tritium gas. The median energy loss from elastic scattering amounts to $\overline{\Delta E}_{\mathrm{el}} = 2.3\,\mathrm{meV}$ [11], which is negligible in the KATRIN measurement. The predominant processes for the KATRIN experiment are inelastic scatterings, resulting in electronic excitations in combination with rotational and vibrational excitations of the molecule, ionization, and molecular dissociation.

Data from detailed measurements is only available for the scattering of 25-keV electrons on molecular hydrogen gas [14,15]; these direct measurements of the energy-loss function were made with energy resolutions down to 40 meV. In these measurements, the contribution of three different groups of lines can be discerned, which are created from the excitations of the $(2p\sigma\ ^1\Sigma_u^+)$, $(2p\pi\ ^1\Pi_u)$, and $(3p\pi\ ^1\Pi_u)$ molecular states around 12.6 eV and 15 eV, respectively.

Aseev et al. [12] and Abdurashitov et al. [13] report on the measurements of energy losses of electrons in gaseous molecular hydrogen, deuterium, and tritium. The shape of the energy-loss function was evaluated by fitting an empirical model to the integral energy spectra obtained with a mono-energetic electron source which generated a beam of electrons with kinetic energies near the endpoint energy of the tritium β-decay. Because of the low energy resolution of several eV, the shape of the energy-loss function was coarsely approximated by a Gaussian to represent electronic excitations and dissociation, and a one-sided Lorentzian to represent the continuum caused by ionization of the molecules [12].

2.1 New parametrization

The high-quality data from the first KATRIN energy-loss measurements described in Sect. 3 allows us to improve the parametrization used in Aseev et al. [12] and Abdurashitov et al. [13]. While the experimental energy resolution is not sufficient to resolve individual molecular states, the combined contribution of each of the three groups of states can clearly be discerned in the KATRIN data.

A new parametrization of the energy-loss function was developed to describe the inelastic scattering region between about 11 eV and 15 eV using three Gaussians, each of which is approximating one group of molecular states. The ionization continuum beyond this energy region is described by the relativistic binary-encounter-dipole (BED) model developed by Kim et al. [17]. While the parameters required by this model are only available for the ionization of H_2-molecules [18], by taking into account the ionization thresholds for the different isotopologs [19]

$$E_i(H_2) = 15.433 \, \text{eV}$$
$$E_i(D_2) = 15.470 \, \text{eV}$$
$$E_i(T_2) = 15.486 \, \text{eV}, \tag{1}$$

the shape of the BED model is a good representation for the tritium data, as can be seen from the fit result in Sect. 4.1. The new parametrization of the full energy-loss function is written as:

$$f(\Delta E) = \begin{cases} \sum_{j=1}^{3} a_j \exp\left(-\frac{(\Delta E - m_j)^2}{2\sigma_j^2}\right) & : \Delta E \leq E_i \\ \frac{f(E_i)}{f_{\text{BED}}(E_i)} \cdot f_{\text{BED}}(\Delta E) & : \Delta E > E_i, \end{cases} \tag{2}$$

where ΔE is the energy loss and a_j, m_j, and σ_j are the amplitude, the mean, and the width of the three Gaussians, respectively. $f_{\text{BED}}(\Delta E)$ is the functional form of the BED model as given in [17] and E_i is the junction point between the two regions given by the ionization threshold. For a smooth

continuation of the model at the junction, the BED function $f_{\text{BED}}(\Delta E)$ is normalized to the local value $f(E_i)$ of the Gaussian components at that position.

3 Measurements

The energy-loss function $f(\Delta E)$ Eq. (2) describes the electron energy losses ΔE from scattering inside the source, which distort the shape of the response function. By measuring the response function, it is possible to determine $f(\Delta E)$. For this, a quasi-monoenergetic and angular-selective photoelectron source ("electron gun"), located at the end of the rear section (see Fig. 1), is used. Guiding the quasi-monoenergetic beam – at a pitch angle of approx. $\theta = 0°$ between the magnetic field lines and the electrons' momentum vector – through the WGTS allows the investigation of the energy loss from scatterings with the source gas molecules stabilized at 30 K. Measuring the electron rate at the focal-plane detector as a function of the electron surplus energy E_s at the analyzing plane (see Eq. (3)) yields the response function of the setup.

The working principle of the electron gun and a general description of the measurement strategy are provided in the following. This is followed by a discussion of the measurement data taken in the two different measurement modes (integral and differential) as well as two important systematic effects in the measurements (pile-up and background).

Electron gun A schematic drawing of the electron gun is provided in Fig. 2. The electrons are generated by photoelectric emission when ultraviolet light is shone through an approximately 30-nm-thick gold photocathode, which is installed inside two electrically charged parallel plates. The photoelectrons are accelerated by a potential difference of 4 kV between the plates separated by 10 mm; the electrons exit the setup through a hole in the front plate (see Fig. 2). This first non-adiabatic acceleration collimates the beam of photoelectrons in a cosine distribution [20] initially. By tilting the plates by the angle α, well-defined pitch angles θ can be obtained. A pitch angle of $\theta = 0°$, which is reached by aligning the plates with the magnetic field lines, is used in the measurements. The generated electrons are further accelerated by a cascade of cylinder electrodes to the desired kinetic energy. The working principle is explained in more detail in [16]. The energy profile of the generated beam depends on the work function Φ of the photocathode and the wavelength λ of the light source.

For the measurements in this work, a 266 nm pulsed UV laser[1] with pulse widths of less than 18 ns (FWHM) is used. The Q-switch of the laser can be externally triggered, which

---

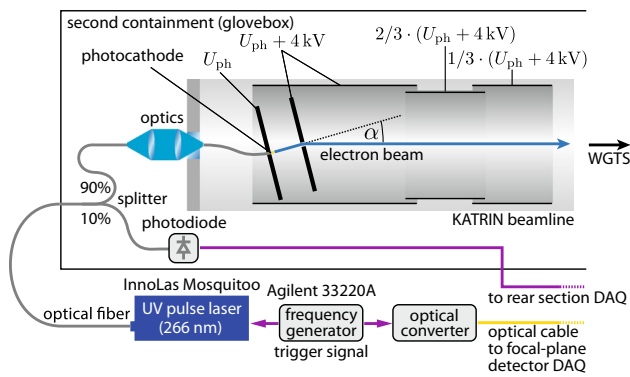[1] InnoLas Mosquitoo Nd:YVO₄ 1064 nm (frequency quadrupled).

Fig. 2 A simplified schematic drawing of the electron gun, including the acceleration electrodes as well as the optical setup used to generate the photoelectrons

Table 1 A summary of the number of scans Σ performed at different column densities relative to the nominal value $\rho_0 d$. The corresponding scattering probability μ is also shown. The average number of counts $<N_0>$ per 50-mV bin for the unscattered electrons at $E_s \in$ [2 eV, 10 eV] is provided for the integral dataset, as well as the sum of all unscattered electrons N_0 at $E_s \in [-1 \, \text{eV}, 1 \, \text{eV}]$ for the differential dataset

Column density/$\rho_0 d$	μ	Σ	$<N_0>$
Integral			
0%	0.00	28	204806
14%	0.25	14	88002
41%	0.75	26	112655
86%	1.56	31	62191
Differential			
15%	0.27	33	565316
22%	0.41	23	380633
39%	0.72	23	267829
84%	1.52	28	154460

allows the synchronization of the creation time of the electron pulses with the detector system. This allows the time-of-flight (TOF) of the signal electrons to be measured. The TOF is used for a differential analysis of the data (see Sect. 3.2).

The photon energy of the monochromatic laser light ($h\nu = 4.66$ eV) is only 0.22 eV above the work function $\Phi = 4.44$ eV [21] of the gold photocathode, which results in a measured energy spread of $\sigma_E < 90$ meV.

To generate electrons with well defined kinetic energies close to the tritium endpoint, voltages down to -21 kV can be applied to the photocathode and cylinder electrodes. The photocathode potential U_{ph} is varied to produce electrons with different surplus energies E_s with respect to the negative main spectrometer retarding potential U_0:

$$E_s = q \cdot U_s + h\nu - \Phi_i = q \cdot (U_{ph} - U_0) + h\nu - \Phi_i , \quad (3)$$

taking into account the additional initial energy of the electrons given by the difference of the photon energy $h\nu$ and the work function Φ_i of the electrons populating different energy levels in the solid (neglecting further solid-state effects). The total initial kinetic energy of the electrons is given as $E_{kin} = q \cdot U_{ph}$.

Measurement approach To resolve the fine structures of the response function, small voltage steps on the order of 0.1 eV are required over the analysis interval of $E_s = -5$ eV to 60 eV. Multiple fast voltage sweeps in alternating directions are preferred to compensate for systematic uncertainties associated with the scan direction and long-term instabilities of the setup. A single high-voltage setpoint adjustment of the main spectrometer requires more than 10 s to stabilize, which does not allow repeated measurements within a reasonable time. For faster measurements, the surplus energy of the electron beam is modified by performing voltage sweeps of U_{ph} while the filter potential of the main spectrometer is kept fixed at $U_0 = -18575$ V. The electron energy is chosen to be slightly above the tritium end-

point energy to avoid β-electron backgrounds but close to the region of interest to minimize effects from the energy dependence of the scattering cross section.

Changing the kinetic energy of the electrons results in a small change of the total inelastic scattering cross section σ_{inel}^{tot} of up to 0.27% over the scanned energy range. This is considered later in the data analysis.

Each sweep (called "scan" in the following) took 30 min and was repeated in alternating scanning directions for approximately 12 h. The obtained rates as a function of the continuous voltage ramp were binned to obtain discrete energy values for the analysis. The data taking was performed in integral and differential modes, which are described in more detail in the following.

3.1 Integral measurements

In the standard KATRIN measurement mode, only electrons with high enough surplus energies to overcome the main spectrometer retarding potential reach the detector. By changing the kinetic energy of the electrons and keeping the retarding potential at a fixed value, the integral response function was measured. A set of integral measurements at three different non-zero column densities as well as one reference measurement at zero column density (see Table 1) were performed. The pulse frequency of the laser was set to 100 kHz, which results in an estimated mean value of 0.05 generated electrons per light pulse.

The individual scans were both corrected for rate intensity fluctuations and detector pile-up (see Sect. 3.3). The former are caused by fluctuations of the laser intensity, which is stable to 1.2%h^{-1}. The light intensity is continuously monitored by a photodiode connected to a fiber splitter, which
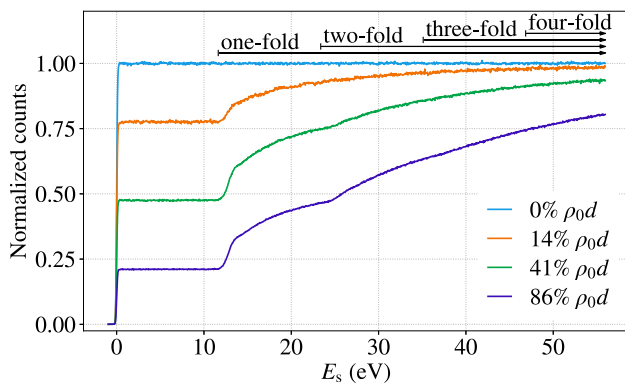
Fig. 3 The measured response functions in integral mode at different fractions of the nominal column density $\rho_0 d$. The response functions are normalized by the electron rate of the reference measurement with an empty source (blue curve). The arrows indicate the energy region where n-fold scattering takes place

Fig. 4 The differential measurements of the time of flight τ (top) and its one-dimensional projection on the electron surplus energy E_s axis (bottom) at 86% of nominal column density. The dashed line marks the lower boundary of the TOF selection at $\tau_{cut} = 35\,\mu s$. The bottom panel shows all events in the TOF selection

is installed just before the light is coupled into the vacuum system of the electron gun (see Fig. 2). The light intensity correction is done by dividing the measured FPD rate by the relative deviation of the light intensity to its mean intensity. The precision of the measured light intensity with this monitoring system is 0.4% and is propagated into the uncertainties of the correction. Data from scans at the same column density are accumulated (Fig. 3). The resulting integral response functions are superpositions of n-fold scattering functions, as indicated in the figure by arrows above the measurement data.

3.2 Differential (time-of-flight) measurements

The time of each trigger pulse for the laser is saved in the detector data stream and used to define the electron-emission time at the electron gun. For each event at the detector, its time difference to the laser pulse is calculated. The time difference corresponds to the time-of-flight (TOF) of the electron through the KATRIN beamline from the electron gun to the detector, including delays for the signal propagation and processing on the order of 1 μs. The knowledge of the electron's time-of-flight can be used as additional information on its kinetic energy.

The negative retarding potential in the main spectrometer U_0 acts as a barrier for the electrons, slowing them down and only allowing electrons with surplus energies $E_s > 0$ to pass through (high-pass filter). The higher the electrons' surplus energy, the less they are slowed down inside the main spectrometer; connecting their flight time through the main spectrometer τ to their surplus energy by $\tau \sim \frac{1}{\sqrt{E_s}}$ [22].

Selecting only electrons with $\tau > \tau_{cut}$ is equivalent to a low-pass filter on E_s [23]. Applying this TOF selection, the high-pass filter main spectrometer is transformed into a
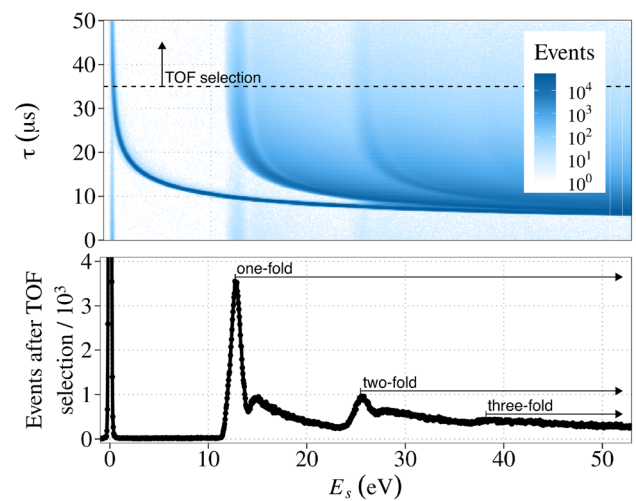
narrow band-pass filter for measuring the differential energy spectrum.

For the differential measurements, the laser was pulsed at 20 kHz to be able to distinguish flight times up to 50 μs between the pulses (see Fig. 4). In this mode, an estimated 0.35 electron per pulse are emitted. Measurements at four different column densities were performed, which are listed in Table 1. Figure 4 shows the measurements at 86% nominal column density $\rho_0 d$ as an example. The top panel shows the time-of-flight versus surplus energy. Here the unscattered electrons as well as one-fold and two-fold scattered electrons are prominently visible as hyperbolic structures.

A TOF selection of events with flight times longer than $\tau_{cut} = 35\,\mu s$ is applied to obtain a differential spectrum, which is projected on E_s and shown in the bottom panel. τ_{cut} is chosen such that an energy resolution of ≈ 0.02 eV is achieved. Higher τ_{cut} allows for a higher energy resolution but results in significantly lower statistics. The vertical features – at 0 eV, 12.5 eV, and 25 eV – for $\tau < 25\,\mu s$ are electrons with flight times $> 50\,\mu s$ from a previous laser pulse. These events are neglected in the analysis.

All events with τ in the range of 35–50 μs are selected and corrected for laser intensity fluctuations analogous to the integral analysis. The energy scale for each measurement is constructed using the measured ramping speed of the high voltage and the position of the peak of unscattered electrons set to $E_s = 0$.

3.3 Pile-up correction

The focal-plane detector is optimized to count single-electron events with an energy resolution of $\Delta E_{FPD} \approx 2$ keV. Due to

the high electron rate of the electron gun ($\approx 10^4$ cps) and the use of a single detector pixel, pile-up effects become relevant. Furthermore, the pulsed electron beam with < 18 ns FWHM windows creates a non-Poisson time distribution compared to a constant wave light source.

The electron flight time depends on the retarding potential and the energy loss from scatterings inside the WGTS. The time difference of the electrons from the same pulse arriving at the detector is thus modified as a function of the surplus energy. For arrival-time differences shorter than the shaping time ($L = 1.6\,\mu$s) of the trapezoidal filter used for pulse shaping of the detector signal, the electrons are counted as one single event with correspondingly higher event energy E_{FPD} (Fig. 5). The number of electrons within the same detector event is denoted as event multiplicity $\mathcal{M}$. As the peaks for different multiplicity $\mathcal{M}$ events overlap in the E_{FPD} histogram, a simple estimation of $\mathcal{M}$ based on E_{FPD} is not possible. Processing the event signal with two additional stages of trapezoidal filters allows more information on the signal shape, such as the bipolar width $\mathcal{W}$ (i.e. the time difference of two consecutive zero crossings of the third trapezoidal-filter output), to be obtained [3]. Electrons with arrival-time differences close to the shaping time distort the trapezoidal output of the first filter stage and thus change the determined bipolar width as a function of the arrival-time difference. With the additional information on the pulse shape, these ambiguities can be resolved and $\mathcal{M}$ can be estimated. The multiplicity estimate $\hat{\mathcal{M}}(E_{\mathrm{FPD}}, \mathcal{W})$ is obtained from Monte Carlo simulations of the detector response for random combinations of $\mathcal{M}$ electrons arriving within the shaping time L. The estimate $\hat{\mathcal{M}}(E_{\mathrm{FPD}}, \mathcal{W})$ is not necessarily identical to $\mathcal{M}$ as there are still remaining ambiguities, which are considered in the uncertainty propagation (see Sect. 4.2). In the case of the integral measurement data, the correction is made by weighting each event with the estimator value. For the differential measurements, no pile-up correction is required, but a $\hat{\mathcal{M}}(E_{\mathrm{FPD}}, \mathcal{W}) > 1$ cut is applied for background suppression (see Sect. 3.4).

A comparison of the integral response function before and after pile-up correction is provided in Fig. 6 to demonstrate its dependence on the surplus energy at two different values of ρd. The dependence of $\hat{\mathcal{M}}(E_{\mathrm{FPD}}, \mathcal{W})$ on the kinetic energy of the electrons over the measurement range of 60 eV is neglected in the correction and an average estimate is used instead. The uncertainty due to the correction method was evaluated with a full simulation of the detector response for each of the response functions measured in integral mode. This yields a correction stability at 5×10^{-4}, which is considered as a systematic uncertainty for the energy-loss function determination.
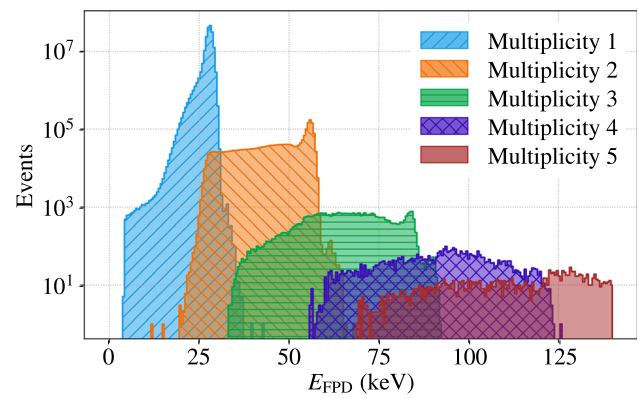

Fig. 5 Reconstructed event energy in the focal-plane Si-detector for all events accumulated during the integral response function measurements at 86% nominal column density $\rho_0 d$. The decomposition with the dedicated pile-up correction method shows that the different multiplicity regions overlap. This effect does not allow for a simple pile-up correction based on event energy alone

3.4 Backgrounds

As the rear section is directly connected to the WGTS, tritium migration upstream towards the electron gun cannot be completely prevented. Tritium can decay within the acceleration fields of the electron gun. Ions created from the β-decays are accelerated towards the photocathode, where their impact can generate multiple secondary electrons simultaneously. Those electrons are accelerated to the same energy as the signal photoelectrons. The kinetic energy of the background electrons changes along with the change of the photocathode voltage U_{ph} in a scan. This results in a background spectrum following the shape of an integral response function, as it is shown in Fig. 7. The background electrons only differ in their initial energy distribution and the emission multiplicity (i.e. the number of electrons generated from an ion impact). The mean energy m_{Bg} and the Gaussian width w_{Bg} of the initial energy distribution of the secondary electrons can be obtained by performing a combined fit to the three background measurements using the same integral response-function model as described in Sect. 4. The initial energy distribution dominates the spectral shape of the transmission function $T(E_{\mathrm{s}})$, which describes the transmission probability of the electrons inside the main spectrometer as a function of the surplus energy E_{s}. The transmission function can be approximated with an error function using m_{Bg} and w_{Bg} as free parameters. The nine energy-loss function parameters were fixed to preliminary evaluated values during the fit. The best-fit result yields

$$m_{\mathrm{Bg}} = 2.42(3)\,\mathrm{eV} \quad \text{and} \quad w_{\mathrm{Bg}} = 2.05(4)\,\mathrm{eV}. \qquad (4)$$
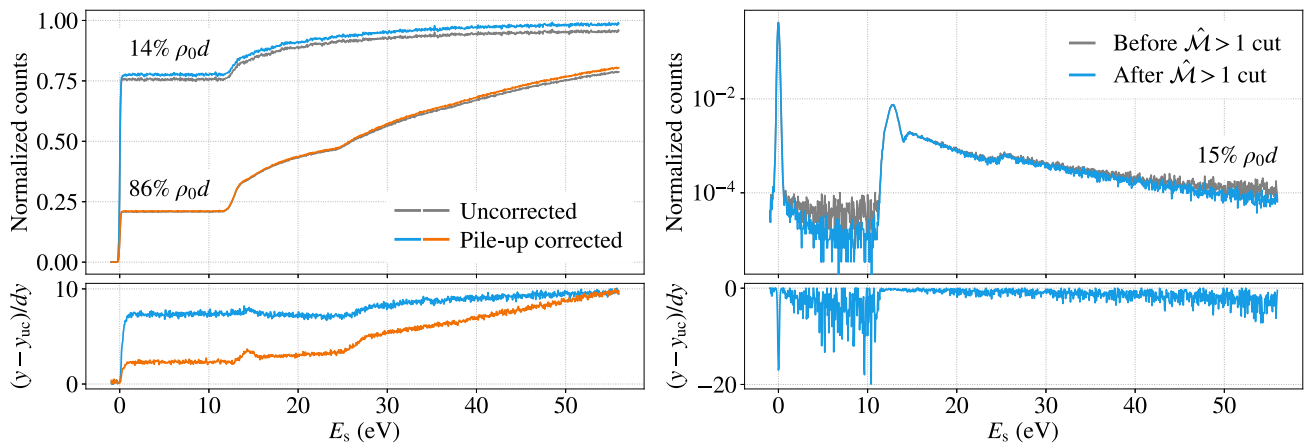
Fig. 6 Left: Selection of measured response functions in integral mode before (grey line) and after (colored line) pile-up correction. The correction removes spectral shape distortions up to ten times larger than the statistical uncertainties. Right: Differential response function before and after applying the $\hat{\mathcal{M}} > 1$ cut. The cut reduces the background component by up to a factor of two without significantly influencing the shape of the signal component. Bottom: The difference between the uncorrected/uncut (uc) data and the corrected/cut data normalized to the data point uncertainties dy

The electron multiplicity distribution of the ion-induced events follows a Poisson distribution (including ion-induced events with no electrons being emitted) with the mean value

$$\hat{S} = 1.3(4). \tag{5}$$

Background events cause a larger detector pile-up effect compared to the signal electrons generated by the pulsed laser, especially in the differential data. The remaining events after the TOF selection are nearly unaffected by detector pile-up, since only the scattered electrons survive. As the arrival time of scattered electrons is delayed compared to other unscattered electrons from the same light pulse, they do not arrive at the detector in time coincidence with other electrons. This allows the multiplicity estimator $\hat{\mathcal{M}}(E_{\text{FPD}}, \mathcal{W})$ to discriminate background events from signal electrons. By excluding events with $\hat{\mathcal{M}} > 1$ in the analysis, the background component can be reduced by about a factor of two without any significant distortion of the signal component. A comparison of the differential response function (at 15% $\rho_0 d$) before and after applying the multiplicity cut is provided in Fig. 6, showing the reduction of the background component. However, the multiplicity $\hat{\mathcal{M}} > 1$ cut causes a distortion of the shape of the background component, which is determined from simulations. The resulting response functions of the background component after an event multiplicity cut are displayed in Fig. 8. The four simulated spectra of the background components for the individual column densities are included in the fit model.

4 Analysis

The energy-loss parameters in Eq. (2) are extracted with a χ^2-fit to multiple datasets in integral and differential mode at dif-
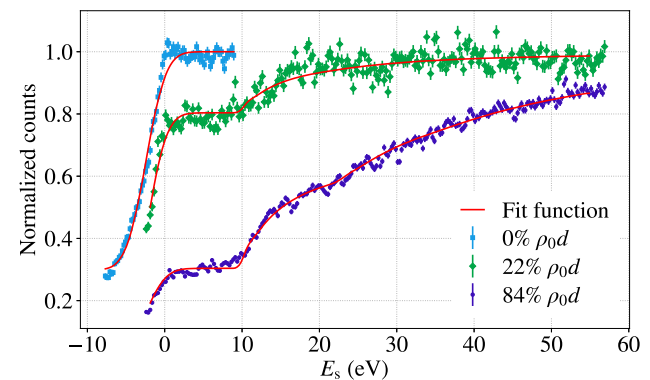

Fig. 7 Background measurements of the electron gun with the light source turned off at different fractions of the nominal column density $\rho_0 d$. Background electrons generated on the emission electrode of the electron gun show similar energy and column density dependencies as signal electrons. Compared to signal electrons, the background energy distribution is broader and shifted towards higher initial values. A combined fit to the data (red line) is used to determine the mean position m_{Bg} and the width w_{Bg} of the initial energy distribution. For better illustration, the shown data is normalized such that the region of unscattered electrons in the plateau at $E_s \in [0\,\text{eV}, 8\,\text{eV}]$ equals $P_0(\mu)$

ferent column densities. The systematic uncertainties in the energy-loss function (for example, those due to the measurement conditions, pile-up and background effects) are determined with Monte Carlo simulations (cf. Sect. 4.2). Results are given for molecular tritium and deuterium source gases below.

4.1 Combined fit of the datasets

The fit model is constructed with the energy-loss function, effects of multiple scatterings in the source, energy smearing in the experimental setup, and the described background
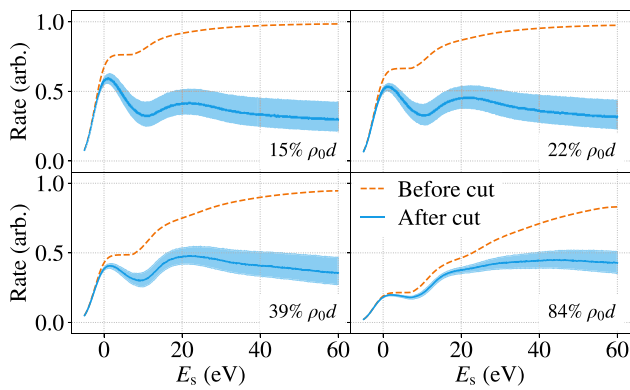
Fig. 8 Simulated background spectra with and without multiplicity $\hat{\mathcal{M}} > 1$ cut for the differential mode after applying the TOF selection. The background spectra without multiplicity cut (orange) show the shape of an integral response function (cf. Fig. 3). The TOF selection (not shown) does not affect this shape of background electrons. The background spectra after multiplicity cut (blue) are strongly reduced but are deformed in shape. The shaded areas show the 1σ intervals resulting from the uncertainty on the mean emission multiplicity $\hat{S}$ of the ion events provided in Eq. (5)

component. The energy-loss function describes a single electron scattering. The probability for n-fold scattering follows a Poisson distribution and is given by

$$P_n(\mu) = \frac{\mu^n}{n!} \exp(-\mu) ,$$ (6)

with the expected mean number of scatterings μ given by

$$\mu = \rho d \cdot \sigma_{\text{inel}}^{\text{tot}}(qU_0).$$ (7)

ρd is the column density during the individual measurements and $\sigma_{\text{inel}}^{\text{tot}}$ is the total inelastic scattering cross section. To correct for the inelastic scattering cross section at different kinetic energies, the parameter μ is scaled by the ratio $\sigma_{\text{inel}}^{\text{tot}}(E_{\text{kin}})/\sigma_{\text{inel}}^{\text{tot}}(qU_0)$, which gives $P_n(\mu, E_s)$. The effects of elastic scattering off tritium can be neglected since the amount of energy transferred in these scattering processes ($\overline{\Delta E}_{\text{el}} = 2.3$ meV [11]) is negligible compared to the energy smearing caused, among others, by the width of the kinetic energy distribution of the electrons produced with the electron gun or the finite energy resolution of the KATRIN main spectrometer. The experimental response to electrons that have been scattered n times in the source gas is given by the n-fold convolution of the energy-loss function $f(\Delta E)$ with itself and convolved one time with the experimental transmission function $T(E_s)$, leading to the following definition of the corresponding scattering functions $\epsilon_n(E_s)$

$$\epsilon_0(E_s) = T(E_s) ,$$
$$\epsilon_1(E_s) = T(E_s) \otimes f(\Delta E) ,$$
$$\epsilon_2(E_s) = T(E_s) \otimes f(\Delta E) \otimes f(\Delta E), \ldots ,$$ (8)
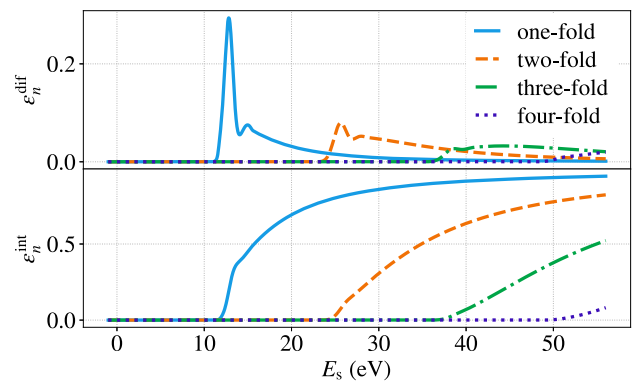

Fig. 9 Differential ($\epsilon_n^{\text{dif}}(E_s)$) and integral ($\epsilon_n^{\text{int}}(E_s)$) scattering functions for up to four-fold scattering

with E_s being the surplus energy of the electrons (see Eq. (3)) and ΔE being the energy loss resulting from an inelastic scattering. The shape of the ionization tail of the energy-loss function is corrected for the shape distortion ($< 10^{-2}$%) caused by the change of the kinetic energy.

The model $R(E_s, \mu)$, which is fit to data, is the sum of the scattering functions $\epsilon_n(E_s)$ weighted by the corresponding Poissonian probabilities

$$R(E_s, \mu) = \sum_{n=0}^{4} P_n(\mu, E_s) \cdot \epsilon_n(E_s).$$ (9)

Given that the surplus energies considered in the energy-loss analysis are limited to $E_s \leq 56$ eV, the highest scattering order that needs to be considered is $n = 4$.

In the integral measurement, the shape of the experimental transmission function $T_{\text{int}}(E_s)$ is obtained from the response function with an empty source volume; Eq. (9) collapses to $R(E_s, 0) = T(E_s)$. $T(E_s)$ is modeled with an error function. Similarly, the transmission function for the differential data $T_{\text{dif}}(E_s)$ could be obtained from a TOF measurement with an empty source. However, it is simply given by the shape of the peak of unscattered electrons observed at non-zero column densities; no additional measurement is required in this case. Thus, we directly use the measurement data to construct the fit model. Figure 9 shows the scattering functions constructed for the differential ($\epsilon_n^{\text{dif}}(E_s)$) and the integral ($\epsilon_n^{\text{int}}(E_s)$) measurement modes for the first four scattering orders.

In addition to the nine parameters in the energy-loss model in Eq. (2) (amplitude, mean and width of the three Gaussians contained in the model), several nuisance parameters are included in the combined fit to differential and integral datasets taken at different column densities. These nuisance parameters include normalization factors $c_i^{\text{dif(int)}}$, mean scattering probabilities $\mu_i^{\text{dif(int)}}$, and background amplitudes $b_i^{\text{dif(int)}}$ for each differential (integral) dataset that is added to
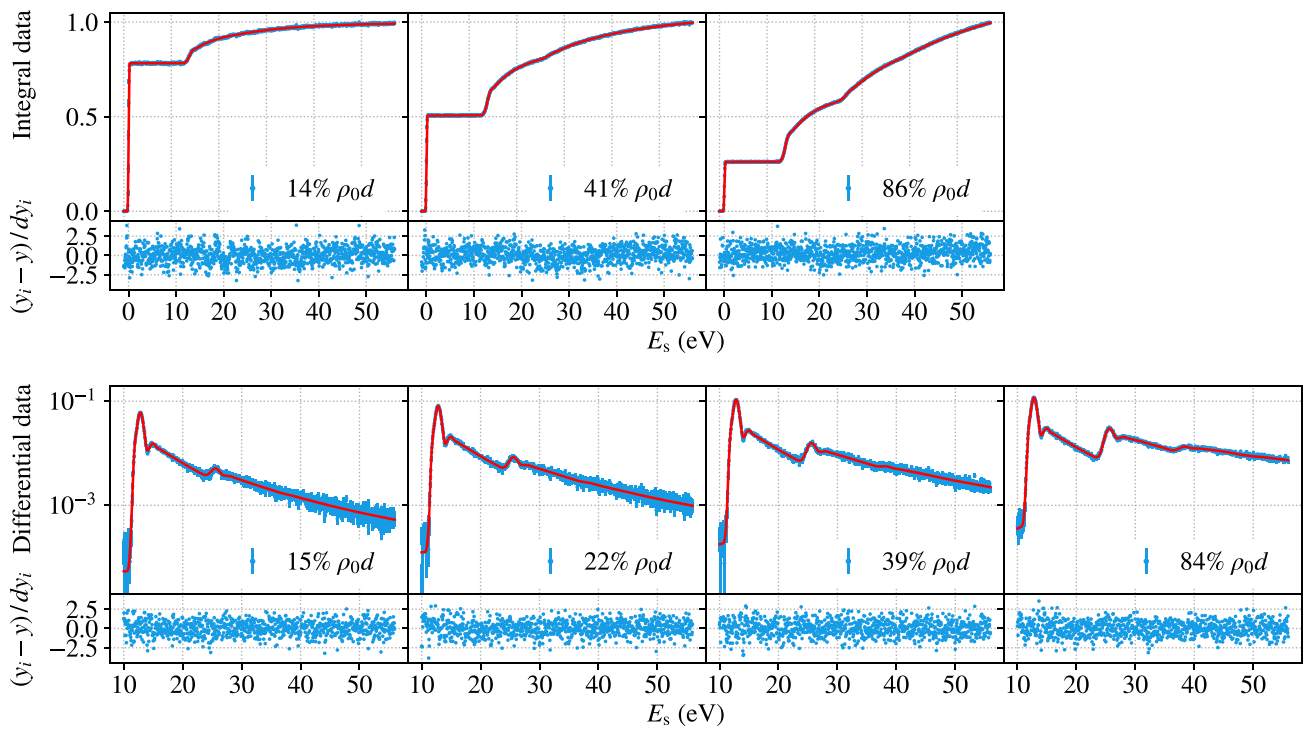
Fig. 10 Results of the combined fit to the differential and integral datasets at different column densities. Each panel shows the data points (blue) and the best-fit result (red) in the upper part and the corresponding residuals in the lower part. A normalization is applied to each of the differential and integral response functions. The differential data is normalized by the total number of counts within the fit range and the integral data by the number of counts in the last bin

the fit. In the fit, we minimize the following χ^2 function for the vector of free fit parameters $\mathcal{P}$

$$\chi^2(\mathcal{P}) = \sum_i^{N_{\text{dif}}} \sum_j \left(\frac{c_i^{\text{dif}} R^{\text{dif}}(E_{s,j}, \mu_i^{\text{dif}}) + b_i^{\text{dif}} B^{\text{dif}}(E_{s,j}, \mu_i^{\text{dif}}) - y_{i,j}^{\text{dif}}}{dy_{i,j}^{\text{dif}}} \right)^2$$
$$+ \sum_i^{N_{\text{int}}} \sum_j \left(\frac{c_i^{\text{int}} R^{\text{int}}(E_{s,j}, \mu_i^{\text{int}}) + b_i^{\text{int}} B^{\text{int}}(E_{s,j}, \mu_i^{\text{int}}) - y_{i,j}^{\text{int}}}{dy_{i,j}^{\text{int}}} \right)^2$$
$$+ \left(\frac{\int_0^{E_{\text{max}}} f(\Delta E) d(\Delta E) - 1}{\delta} \right)^2, \quad (10)$$

where $N_{\text{dif(int)}}$ are the number of differential (integral) datasets considered. $y^{\text{dif(int)}}$ and $dy^{\text{dif(int)}}$ represent the individual data points and their uncertainties. The index of summation j denotes the data points of the individual datasets. The first summand of Eq. (10) describes the contribution of the differential datasets to the χ^2 value. The fit range for the differential datasets extends from 10 eV to 56 eV, excluding the zero-scatter peak and the adjacent background region, which do not contain information on the energy-loss function. The second summand describes the contribution of integral datasets with the fit range of −1 to 56 eV.[2] The ion-induced background component (see Sect. 3.4) is considered

in both summands. For the integral measurements, the shape of the background component $B^{\text{int}}(E_{s,j}, \mu_i^{\text{int}})$ is described by an integral response function (see Fig. 7), but with a different initial energy distribution than the signal electrons. For the differential measurement, $B^{\text{dif}}(E_{s,j}, \mu_i^{\text{dif}})$ is more complex and is obtained from simulations described in Sect. 3.4 and depicted in Fig. 8. The third summand is a pull term that ensures a proper normalization of the fitted energy-loss function up to $E_{\text{max}} = (E_{\text{kin}} - E_i)/2$ with a desired precision of $\delta = 10^{-4}$.

With the definition of the χ^2 given in Eq. (10), a combined fit to four differential datasets and three integral datasets taken at different column densities (see Table 1) was performed. The results are displayed in Fig. 10 for each of the differential and integral datasets included in the fit.

The corresponding best-fit parameters of the energy-loss function are given in Table 2. The fit has a reduced χ^2 value of 1.13(2). A deviation from $\chi^2/N_{\text{dof}} = 1$ can arise from an imperfect semi-empirical parametrization of the energy-loss function or an underestimation of uncertainties. We do not observe significant structures in the fit residuals in Fig. 10 and thus inflate the uncertainties of the data points by $\sqrt{\chi^2/N_{\text{dof}}}$ to achieve a $\chi^2/N_{\text{dof}} = 1$ [24]. The statistical uncertainties from the fit are included in the third column of Table 2 with the covariance matrix shown in Table 5 in

---

[2] This extended fit range is required to determine the amplitude of the background component, which is only accessible below the transmission edge at $E_s = 0$ eV.

Table 2 Best-fit parameters for the energy-loss function in molecular tritium as described in Eq. (2). Parameter correlations are provided as a covariance matrix in Table 5 in the Appendix

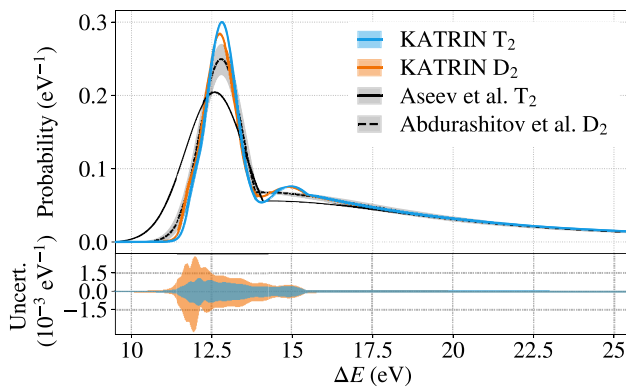| Parameter	Unit	Value
m_1	eV	11.9189(83)
m_2	eV	12.8046(21)
m_3	eV	14.9677(41)
σ_1	eV	0.1836(70)
σ_2	eV	0.4677(22)
σ_3	eV	0.907(13)
a_1	eV^{-1}	0.0328(12)
a_2	eV^{-1}	0.29570(68)
a_3	eV^{-1}	0.07575(37)

Fig. 11 A comparison of the energy-loss functions in D_2 and T_2 from this work and previous measurements of Aseev et al. [12] and Abdurashitov et al. [13]. The y-axis indicates the probability density normalized in $\Delta E \in [0, E_{max}]$ for energy losses ΔE due to inelastic scattering. The Gaussian 1σ uncertainty bands are indicated by the shaded areas[3]. Since the uncertainty of the KATRIN T_2 and D_2 results are too small to be visible in the top plot, the uncertainties are additionally shown in absolute values in the bottom plot

the Appendix. Compared to the empirical energy-loss models of Aseev et al. and Abdurashitov et al. superimposed on our results in Fig. 11, the KATRIN result provides a better energy resolution and reduced uncertainties. As a consistency check, we extrapolate the energy-loss function (fitted up to 56 eV) to $E_{max} = 9.280$ keV yielding a mean energy loss of $\overline{\Delta E}(T_2) = 30.79(1)_{fit}$ eV, which agrees well with the value of 29.9(10) eV reported by Aseev et al. [12].

4.2 Systematic uncertainties

Systematic uncertainties are not included in the combined fit; they are determined separately by a Monte Carlo (MC)

---

[3] The uncertainty band of the Aseev et al. [12] result is significantly smaller than the uncertainty band of the Abdurashitov et al. [13] result. However, the position of the Gaussian kernel was fixed to 12.6 eV in the analysis of Aseev et al.

simulation framework. The framework generates many MC samples, each composed of a detailed simulation of all integral and differential datasets. The systematic effects under investigations can be folded into these MC sets individually, or combined, with or without statistical fluctuation of the count rates included. The underlying response function, on which the MC generation is based, is taken from the best-fit values given in Table 2.

The considered systematic uncertainties cover known effects that arise from the measurement conditions and effects specific to the integral or differential analysis. All systematic effects are shown in Table 3. Their implementation in MC generation is described in the following.

- *Transmission-function model* In order to obtain an analytical description of the integral transmission function $T(E_s)$ for the construction of the integral response-function model, an error function is fit to a reference measurement with an empty WGTS. The error function models the electron's surplus energy threshold needed for transmission in the main spectrometer $m_E = -0.2(29)$ meV and the energy spread

  $w_E = 90(2)$ meV due to the angular and energy distribution of the electron gun and the energy resolution of the main spectrometer. To investigate the uncertainty of this analytical model, MC samples of the measurements at different column densities were generated with m_E and w_E drawn from a multivariate normal distribution according to the best-fit values above with the correlation between them taken into account. No uncertainty on the transmission-function model was considered for the differential data, since the peak of the unscattered electrons from the measurement data is directly used as the transmission function.

- *Column-density drift* As the scattering probability P_n depends on the column density, drifts in the column density during the measurements can cause a distortion of the response function. During the measurements at 41% of the nominal column density, drifts on the order of 0.2%h^{-1} were visible. The reduced stability was caused by CO and tritiated methane freezing inside the injection capillaries. The CO and the methane were generated from radiochemical reactions with the stainless-steel surface during the burn-in period of the first tritium operation [1]. The column density is constantly monitored with a throughput sensor, which allows the drift to be modeled precisely in the simulations. To do so, a linear function $\rho(t)$ is fit to the sensor data, yielding the slope of the drift and the corresponding parameter uncertainty. This linear function is used to model the rate drift due to the column density drift with the slope sampled according to its uncertainty.

Table 3 A list of systematic uncertainties. The listed systematics are investigated by MC simulations yielding the contribution to the total parameter uncertainties and the parameter shifts, which are displayed in Fig. 12. The area of the uncertainty band of the energy-loss function caused by individual systematic effects is provided in the second to last column. The resulting parameter shifts due to each systematic effect are quantified in the last column as the area of the absolute deviations of the nominal function and the function given by the parameter means of the systematic variation. See text for more details

Systematic effect	Source of input	Input values	$\frac{\int |\sigma_{\mathrm{sys}}|}{\int |\sigma_{\mathrm{all}}|}$	$\frac{\int |f_0 - f_{\mathrm{sys}}|}{\int |\sigma_{\mathrm{all}}|}$
Transmission-function model	Error function fit to reference measurement	$m_{\mathrm{E}} = -0.2(22)$ meV $w_{\mathrm{E}} = 90(1)$ meV	0.94	0.260
Column-density drift	Throughput sensor	< 0.2%/h modeling according to sensor data	0.015	0.023
Rate drift	Measurement data	< 0.15%/h	0.002	0.004
Background	Bg measurement	$m_{\mathrm{Bg}} = 2.42(3)$ eV $w_{\mathrm{Bg}} = 2.05(4)$ eV	0.032	0.008
Multiplicity cut	Bg measurement and simulation	$\hat{S} = 1.3(4)$	0.153	0.327
Pile-up correction	Simulation	Max. 0.05%	0.166	0.271
Binning	HV sweep	Bin width of 0.05 eV	0.0	0.110
All systematics			1.0	0.395

– *Rate drift* The electron-production rate of the electron gun can drift due to changes in the work function or a possible degradation of the photocathode (e.g. by ion impacts). The number of unscattered electrons is analyzed for each run after correcting for drifts in the light intensity and the column density to monitor for intrinsic long-term rate drifts. Although the rate drift is very small at $\mathcal{O}(0.1\,\%\mathrm{h}^{-1})$, the resulting drift is used to modulate the response functions accordingly.

– *Background* A background component created from secondary electrons by ion impact on the photocathode (cf. Sect. 3.4) adds to the response functions. In the MC simulations, a background component is added with the parameters of the initial energy distribution of the background electrons (see Eq. (4)) sampled according to their uncertainties.

– *Multiplicity cut* The event multiplicity $\hat{\mathcal{M}}(E_{\mathrm{FPD}}, w) > 1$ cut distorts the background shape in the differential measurements (see Fig. 8) depending on the initial electron multiplicity $\hat{S}$ (see Eq. (5)) of the ion impact. In the MC simulations, the value of $\hat{S}$ is sampled according to its Gaussian uncertainty determined from the measurement and the resulting background component is added to the differential data. Distortions on the signal component from the photoelectrons due to the multiplicity cut were investigated by dedicated detector simulations and added to the differential response functions.

– *Pile-up correction* Detector pile-up is a dominant systematic effect for the integral measurements and is corrected with the pile-up reconstruction method described in Sect. 3.3. The efficiency $\zeta(E_s)$ of this pile-up correction method is determined with detector simulations for each data point. The simulated response functions are multiplied by $\zeta(E_s)$ to include the remaining distortions after applying the pile-up correction. The efficiency $\zeta(E_s)$ is varied according to the Gaussian uncertainty determined in detector simulations.

– *Binning* The response functions are measured by continuously ramping the emission energy of the electron gun. For the data analysis, the continuous data stream is binned into 50-meV bins. This binning effect is included in the MC simulations.

A total of 10,000 MC datasets are generated from the distributions of the systematic effects. Every MC dataset is fit and the best-fit values are taken to construct the probability distribution for each of the nine parameters of interest. From these distributions, the parameter uncertainties are determined from the standard deviations. In addition, systematic parameter shifts are determined from the difference between the median of the distribution and the initial input value from the underlying energy-loss function. The results

Fig. 12 A breakdown of systematic uncertainties for all nine individual energy loss parameters as obtained from Monte Carlo simulations. Shown are the total uncertainty (stat. and sys.), the statistical uncertainty (stat. only) as well as the total systematic uncertainty (all sys.). The data points indicate the difference between the fit to data without any systematic effects and the median of the parameter distribution obtained from the fits to 10,000 MC samples with systematic effects. The bars indicate the standard deviation of the distributions. The measurement is strongly dominated by the statistical uncertainty. The investigated systematic effects do not significantly contribute to a broadening of the parameter uncertainties nor to a significant shift of their mean values
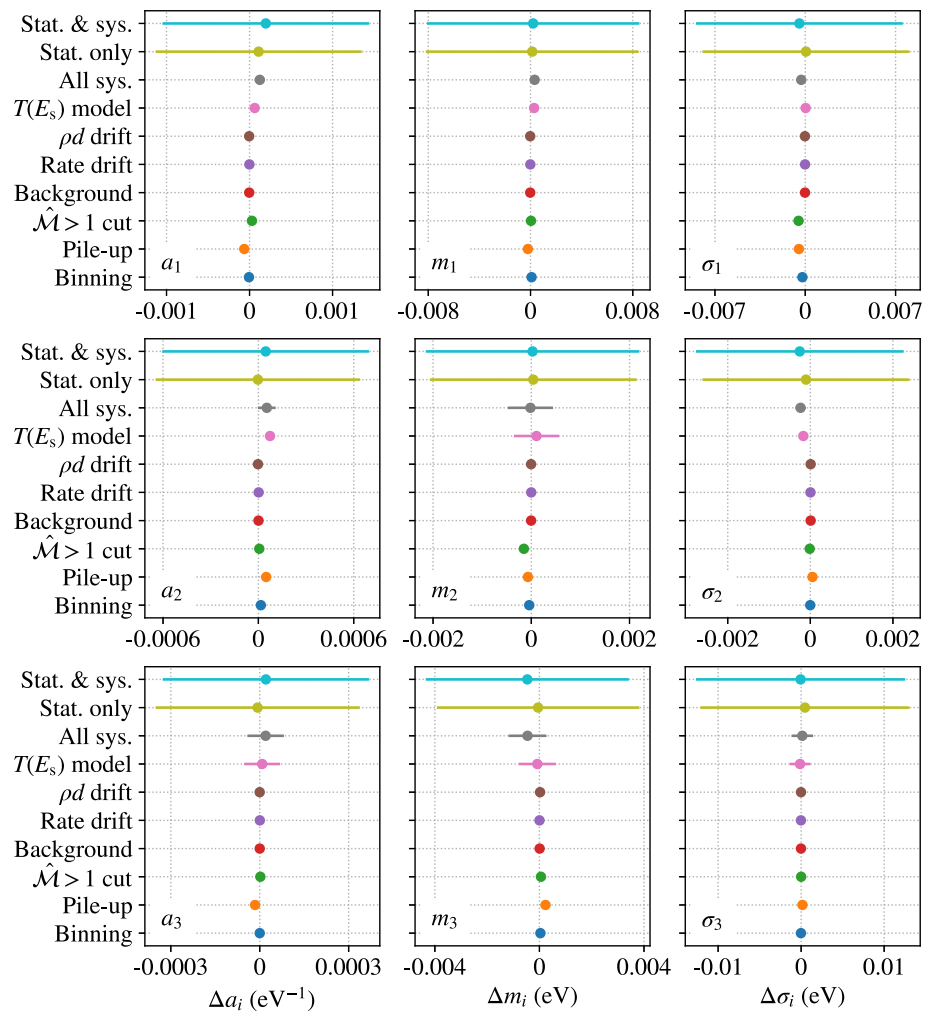
of this evaluation are shown in Fig. 12. The total uncertainty is dominated by the statistics in the data and the widths of the distributions agree well with the parameter uncertainties of the best-fit result provided in Table 2. In order to condense the information of the nine parameter uncertainties for easier interpretation, two metrics are defined. They are shown in the last two columns of Table 3. The first metric, $\int |\sigma_{\text{sys}}| / \int |\sigma_{\text{all}}|$, is the area of the error band in the energy-loss function caused by the specific systematic ($\int |\sigma_{\text{sys}}|$) with respect to the area of the error band caused by all systematic effects ($\int |\sigma_{\text{all}}|$). The error bands originate from the combination of all nine parameter uncertainties. The areas of the error bands are estimates for the uncertainty of the scattering probability over the whole energy range. The second metric, $\int |f_0 - f_{\text{sys}}| / \int |\sigma_{\text{all}}|$, is the area of the difference between the nominal energy-loss function (f_0) and the energy-loss function (f_{sys}) obtained from the simulations including the individual systematic uncertainties. This difference is normalized to $\int |\sigma_{\text{all}}|$. A difference can be created by shifts of the nine parameter values caused by a given systematic

effect. The impact of parameter shifts on the functional form of the energy loss is found to be smaller than the impact of the parameter uncertainties. The dominant contribution to the systematic uncertainty originates from the transmission-function model. Since the total uncertainty of the energy-loss function is dominated by statistical uncertainties in the data and no significant parameter shifts are found, the considered systematic effects are negligible and not further considered in this study.

4.3 Deuterium results

Measurements, similar to the ones described in Sect. 3, were performed with molecular deuterium as source gas in an early commissioning run of the KATRIN experiment. Four integral measurements at 0%, 5%, 35%, and 87% of the nominal source density and a single differential measurement at 5% were made. The data were processed and fit in the same manner as described in Sects. 3 and 4. For the combined χ^2-fit of the deuterium measurements, the best-fit result is obtained

Table 4 Best-fit parameter values for the energy-loss function in molecular deuterium as described in Eq. (2). Parameter correlations are provided as a covariance matrix in Table 6

Parameter	Unit	Value
m_1	eV	11.793(20)
m_2	eV	12.7300(46)
m_3	eV	14.875(11)
σ_1	eV	0.166(17)
σ_2	eV	0.4828(53)
σ_3	eV	1.073(32)
a_1	eV^{-1}	0.0344(28)
a_2	eV^{-1}	0.2737(15)
a_3	eV^{-1}	0.07466(47)

at a reduced $\chi^2 = 1.57(2)$. Similar to the tritium data, the uncertainties of the data points are rescaled by $\sqrt{\chi^2/N_{\mathrm{dof}}}$ to obtain a reduced $\chi^2 = 1$. The parameter values as well as the covariance matrix are provided in Tables 4 and 6. The slightly increased χ^2 value and the larger model uncertainties (cf. Fig. 11) can be explained by the presence of a stronger detector pile-up in the integral data due to an electron rate that was twice as high as that of the tritium measurements combined with the availability of only one differential dataset. A full propagation of the systematic uncertainties was not performed for the deuterium measurements as the simulations for tritium showed that the measurements are strongly dominated by the statistical uncertainty. Furthermore, neither the systematic uncertainty due to methane freezing causing column-density drift nor the background generated from tritium ions is present in the absence of tritium.

Figure 11 shows the minor differences of the energy-loss models for deuterium and tritium, as the electronic excitation states are shifted to lower energies on the order of 100 meV.[4] Extrapolating again to E_{max} the energy loss function results in a mean energy loss of $\overline{\Delta E}(D_2) = 30.64(1)_{\mathrm{fit}}$ eV, for the dominant deuterium isotopologs. This mean energy-loss value is 0.15 eV smaller than for tritium isotopologs, but we should not forget that we extrapolate the energy-loss function in energy by a factor 200 and we do not account for systematic uncertainties here for this consistency check.[5]

---

[4] Such a difference between the different hydrogen isotopologs is theoretically expected. The observed difference of $\mathcal{O}(100\,\mathrm{meV})$ is in agreement with preliminary calculations in dipole approximation in which the peak positions of the rovibrationally resolved spectra for the $2p\sigma\ ^1\Sigma_{\mathrm{u}}$ and the $2p\pi\ ^1\Pi_{\mathrm{u}}$ states were compared for the isotopes D_2 and T_2 [25].

[5] Just to get an order of magnitude estimate of the systematic uncertainties of the mean energy loss, we have left the junction point E_{i} between the three Gaussians and the BED tail in Eq. (2) free in our fits, yielding already an additional systematic uncertainty on the mean energy loss as big as the discrepancy. We want to add that the systematics of

5 Summary and outlook

A series of precision measurements of the energy-loss function of 18.6-keV electrons scattering off molecular tritium and deuterium gas was performed. The measurements were carried out in the KATRIN setup by using a pulsed beam of monoenergetic and angular selected electrons from a photoelectron source. The measurements were made in integral and differential time-of-flight measurement modes.

A new semi-empirical parametrization of the energy-loss function was developed, which describes the set of electronic states in combination with molecular excitations, dissociation, and ionization better than previous models. This new model is described by nine parameters, which were determined by performing a combined χ^2-fit to both integral and differential measurement data. The measurements and analyses performed in this work achieved a significant improvement over existing empirical energy-loss models in terms of energy resolution and uncertainties. A detailed investigation of the systematic effects shows that the parameter uncertainties are dominated by statistical uncertainties. This allows further improvement in precision in future measurements.

The obtained electron energy-loss function in tritium was used in the analysis of the first KATRIN dataset, which led to an improved upper limit of the effective neutrino mass $m_\nu < 1.1$ eV (90% CL) [26]. For this dataset, recorded at reduced source strength, the uncertainty of the energy-loss model contributes to the systematic uncertainty of the observable m_ν^2 with $\sigma(m_\nu^2) < 10^{-2}$eV^2 and is inconsequential compared to other effects [1]. The achieved precision of the energy-loss function is close to the target effect of $\sigma(m_\nu^2) < 7.5 \times 10^{-3}$eV^2 [2] that is necessary for reaching the final KATRIN sensitivity of $m_\nu = 0.2$ eV (90% CL).

---

this extrapolation is not critical for the determination of the energy-loss function in our interval of interest [0 eV, 54 eV].

Data Availability Statement This manuscript has no associated data or the data will not be deposited. [Authors' comment: Further analyses of the measurement data are subject of a dissertation in preparation.]

Availability of data and material The datasets generated during and/or analysed during the current study are available from the corresponding author on reasonable request.

Declarations

Conflict of interest The authors have no relevant financial or non-financial interests to disclose.

Code availability Not available.

Appendix

See Table 5.

Table 5 Covariance matrix for the parametrization of the energy-loss function for molecular tritium, as provided in Table 2

	m_1	m_2	m_3	σ_1	σ_2	σ_3	a_1	a_2	a_3
m_1	6.941×10^{-5}	1.034×10^{-5}	-3.388×10^{-6}	4.537×10^{-5}	-7.980×10^{-6}	8.094×10^{-6}	4.529×10^{-6}	-6.505×10^{-7}	-6.581×10^{-8}
m_2	1.034×10^{-5}	4.503×10^{-6}	7.403×10^{-7}	8.265×10^{-6}	-1.206×10^{-6}	-8.627×10^{-6}	1.342×10^{-6}	2.262×10^{-7}	1.893×10^{-7}
m_3	-3.388×10^{-6}	7.403×10^{-7}	1.641×10^{-5}	-4.727×10^{-6}	3.464×10^{-6}	-2.255×10^{-6}	-1.004×10^{-6}	-1.272×10^{-7}	-6.165×10^{-7}
σ_1	4.537×10^{-5}	8.265×10^{-6}	-4.727×10^{-6}	4.858×10^{-5}	-8.929×10^{-6}	1.503×10^{-5}	2.481×10^{-6}	-9.888×10^{-9}	-1.840×10^{-7}
σ_2	-7.980×10^{-6}	-1.206×10^{-6}	3.464×10^{-6}	-8.929×10^{-6}	4.746×10^{-6}	-1.521×10^{-5}	-1.755×10^{-6}	-5.149×10^{-7}	2.435×10^{-7}
σ_3	8.094×10^{-6}	-8.627×10^{-6}	-2.255×10^{-6}	1.503×10^{-5}	-1.521×10^{-5}	1.632×10^{-4}	3.346×10^{-6}	-2.017×10^{-6}	-4.154×10^{-6}
a_1	4.529×10^{-6}	1.342×10^{-6}	-1.004×10^{-6}	2.481×10^{-6}	-1.755×10^{-6}	3.346×10^{-6}	1.462×10^{-6}	9.769×10^{-8}	-4.513×10^{-8}
a_2	-6.505×10^{-7}	2.262×10^{-7}	-1.272×10^{-7}	-9.888×10^{-9}	-5.149×10^{-7}	-2.017×10^{-6}	9.769×10^{-8}	4.581×10^{-7}	4.877×10^{-8}
a_3	-6.581×10^{-8}	1.893×10^{-7}	-6.165×10^{-7}	-1.840×10^{-7}	2.435×10^{-7}	-4.154×10^{-6}	-4.513×10^{-8}	4.877×10^{-8}	1.354×10^{-7}

Table 6 Covariance matrix for the parametrization of the energy-loss function for molecular deuterium, as provided in Table 4

	m_1	m_2	m_3	σ_1	σ_2	σ_3	a_1	a_2	a_3
m_1	3.883×10^{-4}	5.087×10^{-5}	-2.607×10^{-5}	2.487×10^{-4}	-4.157×10^{-5}	6.592×10^{-5}	1.214×10^{-5}	-4.525×10^{-6}	-3.856×10^{-7}
m_2	5.087×10^{-5}	2.093×10^{-5}	1.873×10^{-5}	4.040×10^{-5}	-2.989×10^{-6}	-5.680×10^{-5}	4.437×10^{-6}	2.116×10^{-6}	4.871×10^{-7}
m_3	-2.607×10^{-5}	1.873×10^{-5}	1.144×10^{-4}	-3.436×10^{-5}	4.237×10^{-5}	-2.466×10^{-4}	-8.612×10^{-6}	5.337×10^{-6}	9.459×10^{-7}
σ_1	2.487×10^{-4}	4.040×10^{-5}	-3.436×10^{-5}	2.793×10^{-4}	-4.330×10^{-5}	6.404×10^{-5}	-4.041×10^{-6}	-7.999×10^{-7}	-5.273×10^{-8}
σ_2	-4.157×10^{-5}	-2.989×10^{-6}	4.237×10^{-5}	-4.330×10^{-5}	2.798×10^{-5}	-1.050×10^{-4}	-7.907×10^{-6}	-2.660×10^{-7}	6.033×10^{-7}
σ_3	6.592×10^{-5}	-5.680×10^{-5}	-2.466×10^{-4}	6.404×10^{-5}	-1.050×10^{-4}	1.033×10^{-3}	1.829×10^{-5}	-2.974×10^{-5}	-1.231×10^{-5}
a_1	1.214×10^{-5}	4.437×10^{-6}	-8.612×10^{-6}	-4.041×10^{-6}	-7.907×10^{-6}	1.829×10^{-5}	7.761×10^{-6}	2.777×10^{-7}	-6.118×10^{-8}
a_2	-4.525×10^{-6}	2.116×10^{-6}	5.337×10^{-6}	-7.999×10^{-7}	-2.660×10^{-7}	-2.974×10^{-5}	2.777×10^{-7}	2.173×10^{-6}	4.225×10^{-7}
a_3	-3.856×10^{-7}	4.871×10^{-7}	9.459×10^{-7}	-5.273×10^{-8}	6.033×10^{-7}	-1.231×10^{-5}	-6.118×10^{-8}	4.225×10^{-7}	2.193×10^{-7}

References

1. M. Aker, et al., Analysis methods for the first KATRIN neutrino-mass measurement (2021). arXiv:2101.05253
2. The KATRIN collaboration, KATRIN design report. FZKA scientific report, vol. 7090 (2005). https://doi.org/10.5445/IR/270060419
3. M. Aker, et al., The design, construction, and commissioning of the KATRIN experiment (2021). arXiv:2103.04755
4. G. Beamson, H. Porter, D. Turner, J. Phys. E Sci. Instrum. **13**(1), 64 (1980). https://doi.org/10.1088/0022-3735/13/1/018
5. V. Lobashev, P. Spivak, Nucl. Instrum. Methods A **240**(2), 305 (1985). https://doi.org/10.1016/0168-9002(85)90640-0
6. A. Picard et al., Nucl. Instrum. Methods B **63**(3), 345 (1992). https://doi.org/10.1016/0168-583x(92)95119-c
7. F. Friedel et al., Vacuum **159**, 161 (2019). https://doi.org/10.1016/j.vacuum.2018.10.002
8. A. Marsteller, B. Bornschein et al., Vacuum **184**, 109979 (2021). https://doi.org/10.1016/j.vacuum.2020.109979
9. C. Röttele, J. Phys. Conf. Ser. **888**, 012228 (2017). https://doi.org/10.1088/1742-6596/888/1/012228
10. J. Amsbaugh et al., Nucl. Instrum. Methods A **778**, 40 (2015). https://doi.org/10.1016/j.nima.2014.12.116
11. M. Kleesiek et al., Eur. Phys. J. C **79**, 3 (2019). https://doi.org/10.1140/epjc/s10052-019-6686-7
12. V.N. Aseev et al., Eur. Phys. J. D **10**(1), 39 (2000). https://doi.org/10.1007/s100530050525
13. D.N. Abdurashitov et al., Phys. Part. Nuclei Lett. **14**(6), 892 (2017). https://doi.org/10.1134/s1547477117060024
14. J. Geiger, Z. Phys. **181**(4), 413 (1964). https://doi.org/10.1007/bf01380873
15. R.C. Ulsh et al., J. Chem. Phys. **60**(1), 103 (1974). https://doi.org/10.1063/1.1680755
16. J. Behrens et al., Eur. Phys. J. C **77**, 6 (2017). https://doi.org/10.1140/epjc/s10052-017-4972-9
17. Y.K. Kim et al., Phys. Rev. A **62**, 5 (2000). https://doi.org/10.1103/physreva.62.052710
18. Y.K. Kim, M.E. Rudd, Phys. Rev. A **50**(5), 3954 (1994). https://doi.org/10.1103/PhysRevA.50.3954
19. P. Weck et al., Phys. Rev. A **60**(4), 3013 (1999). https://doi.org/10.1103/PhysRevA.60.3013
20. Z. Pei, C.N. Berglund, Jpn. J. Appl. Phys. **41**(Part 2, No. 1A/B), L52 (2002). https://doi.org/10.1143/jjap.41.l52
21. R. Sack, Measurement of the energy loss of 18.6 keV electrons on deuterium gas and determination of the tritium Q-value at the KATRIN experiment. Ph.D. thesis, Westfälische Wilhelms-Universität Münster (2020). http://nbn-resolving.de/urn:nbn:de:hbz:6-59069498754
22. N. Steinbrink et al., New J. Phys. **15**(11), 113020 (2013). https://doi.org/10.1088/1367-2630/15/11/113020
23. J. Bonn et al., Nucl. Instrum. Methods A **421**(1), 256 (1999). https://doi.org/10.1016/S0168-9002(98)01263-7
24. P. Zyla et al., Prog. Theor. Exp. Phys. **2020**, 8 (2020). https://doi.org/10.1093/ptep/ptaa104
25. A. El Miniawy, A. Saenz, *private communication; to be published in the Bachelor thesis of A. El Miniawy* (2021)
26. M. Aker et al., Phys. Rev. Lett. **123**, 22 (2019). https://doi.org/10.1103/physrevlett.123.221802